Magnetism and magnetization dynamics in thin film ferromagnets

Verhagen, T.G.A.

CHAPTER 5

Temperature dependence of the Gilbert damping in thin Co/Pt bilayers

5.1 Introduction

In this Chapter, we measure the spin transport between a ferromagnet (F) and a normal metal (N) using the spin pump technique, that was introduced in Chapter 2. When a ferromagnet is capped with an adjacent metal layer and brought into ferromagnetic resonance, the ferromagnet emits a spin current into that layer. From such spin pumping experiments, we can derive the spin mixing conductance $G^{\uparrow\downarrow}$ which is an interface property, and which is a measure for the amount of injected spin current into the adjacent layer. Consequently, the experiment shows whether it is possible at all to inject a spin current.

Originally, we were interested to know whether spin can be transferred to and from a Sm-Co layer and study which properties plays a crucial role in the spin torque and spin pumping phenomena. However, we will use Co thin films which have been capped with the normal metals Pt or Cu to get around the growth related issues of the Sm-Co thin films, which were discussed in the previous Chapter. We are particularly interested in the temperature dependence of the spin transfer by spin pumping, which until now received little attention.

We measure spin pumping using the ferromagnet resonance (FMR) technique, which will be discussed in Section 5.2. Spin pumping can be seen as an extra contribution to the damping and thereby to the linewidth in an FMR experiment if the adjacent layer efficiently removes ('sinks') the spin. Pt is a good spin sink, because the high charge of the nucleus gives rise to strong spin-orbit scattering. This is much less for Cu, which is assumed to be a 'bad' spin sink and can serve as a reference. As discussed in Chapter 2, the basic signature of the spin pumping effect in F/N bilayers is that its contribution to the damping increases inversely proportional to the F-layer thickness. As will be shown below, this can be observed in particular for thicknesses below 10 nm. In our experiments, we typically used values for the thickness of the F-layer between 1 and 20 nm.

Besides the contribution of spin pumping, many other processes contribute to the damping. They can be intrinsic, due to the bandstructure of the material; or extrinsic, caused by inhomogeneities. The first part of this Chapter is concerned with these various processes. Section 5.2 also shows how measurements of the dependence of the linewidth on the angle between the applied magnetic field and the film normal can be used to extract the damping contribution from inhomogeneities, such as the roughness or a spread in the directions of crystalline axes.

Section 5.3 is devoted to intrinsic contributions to the linewidth such as spin-orbit relaxation or inter- and intraband scattering. Section 5.4 gives the experimental details and in Section 5.5, the room temperature FMR characterization and analysis is presented. Spin pumping in the Pt layer can also be detected electrically by the spin Hall effect. This is shown and discussed in Section 5.6. Sections 5.7 and 5.8 present the low temperature conductance and FMR characterization of the Co/Pt bilayers. At low temperatures, we find the same thickness dependence as was observed at room temperature. In Section 5.9, the last section, a full discussion of the data is given.

One note should be made with respect to units. In order to connect better to the existing literature in this field, the choice has been made to present the data in cgs units, rather than in the SI units used in Chapter 4.

5.2 Ferromagnetic resonance in thin magnetic films

The dynamics of the precession of the magnetization can be studied using the ferromagnetic resonance (FMR) technique [131, 132]. From

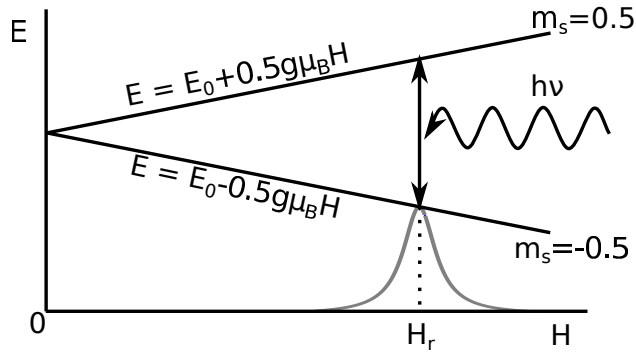

Figure 5.1: Basic principle of EPR and FMR. The degenerate states are split by an external static magnetic field. An applied radio frequency magnetic field can induce a transition between the two states when the resonance condition is fulfilled.

FMR spectra, static and dynamic properties of (ultra)thin magnetic layers can be obtained. From the value of the resonance field in the FMR spectra static magnetic properties such as the g-factor and the magnetic anisotropies can be found. From the FMR linewidth, the magnetic homogeneity and the damping parameter for the magnetization precession can be obtained.

5.2.1 The resonance field

The FMR technique is similar to the electron paramagnetic resonance (EPR) or the nuclear magnetic resonance (NMR) technique. Consider first a single ion with a magnetic dipole with a magnetic moment $\boldsymbol{\mu}$ equal to $\boldsymbol{\mu} = \gamma\hbar\mathbf{L}$, where $\gamma = g\mu_B/\hbar$ is the gyromagnetic ratio. When this magnetic dipole is placed in a static magnetic field $\mathbf{H}$ the corresponding energy E is equal to
E = -$\boldsymbol{\mu}\cdot\mathbf{H}$. When $\mathbf{H}$ points in the (0,0,H)-direction, the energy of the ion is equal to $E = -\gamma\hbar m_s H_0$, where m_s is the spin quantum number and equal to $\pm$ 0.5 for an electron.

When irradiating the dipole with a radio frequency (RF) magnetic field $\mathbf{H}_1$ perpendicular to $\mathbf{H}$, the RF field with frequency ν can induce a transition between both states if the resonance condition

$$h\nu = 2g\mu_B|m_s|H_r, \tag{5.1}$$

is fulfilled as shown in Figure 5.1.

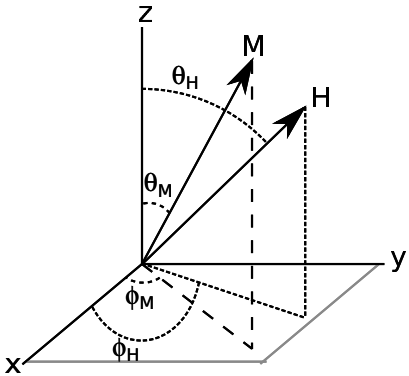

Figure 5.2: The coordinate system used for the analysis of the FMR data. The thin film lies in de xy-plane and the magnetization **M** of the film points in the **M**-direction. The applied DC magnetic field **H** points in the **H**-direction.

In a ferromagnet, the total magnetic moment of the sample can be considered as one macrospin **M**, which precesses around the local static field **H** at the Larmor frequency $\boldsymbol{\omega}_L = \gamma \mathbf{H}$. The macrospin **M** behaves in the same way as the single ion in a static magnetic field, when irradiated with a RF magnetic field, but the ferromagnetic resonance condition is now given by the Smit-Beljars-Suhl equation [133, 134]

$$\frac{\omega}{\gamma} = \frac{1}{M_s \sin\theta_M} \sqrt{\frac{\partial^2 F}{\partial \theta_M^2}\frac{\partial^2 F}{\partial \phi_M^2} - \frac{\partial^2 F}{\partial \theta_M \phi_M}}. \tag{5.2}$$

The angles $\theta_{H/M}$ and $\phi_{H/M}$ are the polar and azimuthal angles of the DC magnetic field **H** and the magnetization **M** with respect to the z- and x-axis, respectively. The coordinate system is shown in Figure 5.2. F is the total energy per unit volume of magnetization and is modeled for a thin film by

$$F = -\mathbf{M}\cdot\mathbf{H} + 2\pi(\mathbf{M}\cdot\mathbf{n})^2 - K(\mathbf{M}\cdot\frac{\mathbf{u}}{M_s})^2. \tag{5.3}$$

Here the first term is the Zeeman energy, the second term the demagnetization energy and the third term the uniaxial anisotropy term, with K the magnetic anisotropy constant, M_s the saturation magnetization and $\mathbf{n}$ and $\mathbf{u}$ the unit vectors normal to the surface of the sample and oriented along the easy axis of the sample, respectively. The

applied magnetic field **H** and the magnetization **M** of the sample can then be written as

$$\mathbf{H} = H(\sin\theta_H \cos\phi_H, \sin\theta_H \sin\phi_H, \cos\theta_H) \tag{5.4}$$

$$\mathbf{M} = M_s(\sin\theta_M \cos\phi_M, \sin\theta_M \sin\phi_M, \cos\theta_M). \tag{5.5}$$

Combining equation (5.3) and (5.2) for the perpendicular anisotropy case (**n** = **u** = [001]), the ferromagnetic resonance condition is

$$\left(\frac{\omega}{\gamma}\right)^2 = \left[H_r\cos(\theta_H - \theta_M) - 4\pi M_{\text{eff}}\cos^2\theta_M\right] \times \left[H_r\cos(\theta_H - \theta_M) - 4\pi M_{\text{eff}}\cos 2\theta_M\right]. \tag{5.6}$$

Here $4\pi M_{\text{eff}}$ = $4\pi M_s$ - $H_\perp$ is the effective demagnetization field and $H_\perp$ = $2K_\perp/M_s$ the perpendicular anisotropy field. The values for θ_M and ϕ_M on resonance can be determined by the condition $\partial F/\partial\theta_M = 0$ and $\partial F/\partial\phi_M = 0$; θ_M on resonance is then given by

$$\sin(2\theta_M) = \frac{2H_r}{4\pi M_s - H_\perp}\sin(\theta_M - \theta_H). \tag{5.7}$$

From equation 5.6, it follows that the resonance conditions, for in-plane and out-of-plane magnetic fields, where $\theta_M = \theta_H$, are equal to

$$\omega = \gamma(H_r - 4\pi M_{\text{eff}}) \qquad \text{out-of-plane} \tag{5.8}$$

$$\omega = \gamma\sqrt{H_r(H_r + 4\pi M_{\text{eff}})} \qquad \text{in-plane.} \tag{5.9}$$

5.2.2 The linewidth

The linewidth of the FMR spectrum has two sources; intrinsic relaxation of the magnetization that is characterized by the Gilbert damping constant α and a relaxation of the magnetization due to sample inhomogeneities. The angular dependence of the FMR spectrum helps to identify the dominant relaxation mechanisms. The in-plane peak-to-peak linewidth $\Delta H_{\text{pp}}^{\parallel}$ and out-of-plane peak-to-peak linewidth $\Delta H_{\text{pp}}^{\perp}$ give clear evidence of the type of damping contributions [135].

Intrinsic relaxation of the magnetization, through mechanisms that will be discussed in the next section, leads to a *homogeneous* broadening of the linewidth $\Delta H_{\text{pp}}^{\text{homo}}$, which is given by [134]

$$\Delta H_{\text{pp}}^{\text{homo}} = \frac{1}{\sqrt{3}}\frac{\alpha}{M_s}\left(\frac{\partial^2 F}{\partial\theta_M^2} + \frac{1}{\sin^2\theta_M}\frac{\partial^2 F}{\partial\phi_M^2}\right)\left|\frac{d(\omega/\gamma)}{dH_R}\right|^{-1}. \tag{5.10}$$

In this case, $\Delta H_{\text{pp}}^{\parallel}$ is equal to $\Delta H_{\text{pp}}^{\perp}$.

Sample inhomogeneities can contribute significantly to the damping of the ferromagnet. The extra damping due to the sample inhomogeneities can be described by the so-called local resonance model with inhomogeneous broadening due to spatial variations in the spread of the crystallographic axis in the θ_H-direction $\Delta(\theta_H)$ and spatial variations of the demagnetization field $\Delta(4\pi M_{\text{eff}})$. This case is encountered for thin films with a perpendicular surface anisotropy or for polycrystalline multilayers. The inhomogenous linewidth broadening $\Delta H_{\text{pp}}^{\text{inhomo}}$ can be described as [136, 137]

$$\Delta H_{\text{pp}}^{\text{inhomo}} = \frac{1}{\sqrt{3}} \left| \frac{dH_r}{d(4\pi M_{\text{eff}})} \right| \Delta(4\pi M_{\text{eff}}) + \frac{1}{\sqrt{3}} \left| \frac{dH_r}{d\theta_H} \right| \Delta(\theta_H), \quad (5.11)$$

where $|dH_r/d(4\pi M_{\text{eff}})|$ and $|dH_r/d\theta_H|$ are deduced from equations 5.6 and 5.7. The total measured linewidth is then the sum of the homogeneous and inhomogeneous linewidth. In this case, $\Delta H_{\text{pp}}^{\parallel}$ is smaller than $\Delta H_{\text{pp}}^{\perp}$.

Finally, when $\Delta H_{\text{pp}}^{\parallel}$ is larger than $\Delta H_{\text{pp}}^{\perp}$, the intrinsic Gilbert damping and an extrinsic two-magnon scattering process are sufficient to describe the experimental data. This case is usually encountered in (ultra)thin films with a good structural order.

5.3 Damping in thin magnetic films

The Gilbert damping is the timescale at which the magnetization aligns with the effective magnetic field H_{eff}. The relaxation can take place in two different ways as shown in Figure 5.3: either the spin angular momentum is transferred to non-magnetic degrees of freedom, which is called direct damping; or the spin angular momentum is transferred to other magnetic degrees of freedom such as spin waves, which is called indirect damping. Significant relaxation processes in thin ferromagnetic films [138] are spin-orbit relaxation damping, two-magnon scattering and eddy current damping, which will be discussed in the next sections.

The temperature dependence of the Gilbert damping α is an almost unexplored area. To our knowledge, Bhagat et al. [42, 139–141] in the nineteen-sixties and -seventies measured the damping of single-crystal whiskers of Co, Fe and Ni using FMR. In the seventies, Heinrich et al. measured the low temperature damping in Ni [142]. They observed that the Gilbert damping is not a monotonously increasing or decreas-

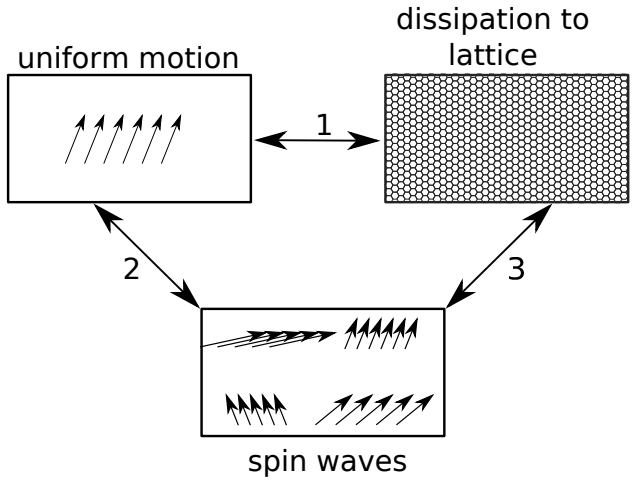

Figure 5.3: Ferromagnetic resonance excites a uniform precession mode in a ferromagnet, that can relax via a direct (path 1) and indirect (via path 2 + 3) relaxation channel. When the relaxation happens via the indirect relaxation channel, energy is transferred to spin waves.

ing function, but that a clear maximum is observed at a finite temperature.

In F/N hybrid structures, Yakata et al. studied the temperature dependence of the spin diffusion length in Cu for multilayer structures Cu/$Ni_{80}Fe_{20}$/Cu(d) and Cu/$Ni_{80}Fe_{20}$/Cu(d)/Pt [143] using the spin pumping technique. Furthermore, Czeschka et al. used also the spin pumping technique to measure the inverse spin Hall voltage of Fe/Pt and Co/Pt thin films [70] and thereby the spin mixing conductance down to low temperatures.

5.3.1 Spin-orbit relaxation damping

In 1967, Kamberský showed [68, 144, 145] that the intrinsic Gilbert damping can be described using a torque-correlation model. A clear introduction to the temperature dependence, which we will follow here, can be found in the thesis of Gilmore [146] and the review of Fähnle and Illg [69]. They used an effective field approach, to provide a better picture of the physical processes involved.

When the spin-orbit interaction is not negligible, $\mathbf{S}$ and $\mathbf{L}$ are no good quantum numbers anymore, because the spin-orbit interaction

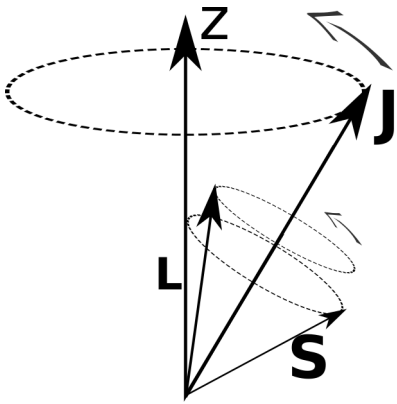

Figure 5.4: The orbital $\mathbf{L}$ and spin $\mathbf{S}$ angular momentum precess around the precessing total angular momentum $\mathbf{J}$.

is proportional to $\mathbf{L} \cdot \mathbf{S}$. The orbital and spin angular momenta exert a torque on each other, that cause them to precesses about a resultant vector $\mathbf{J}$, the total angular momentum. As shown in Figure 5.4, the total angular momentum $\mathbf{J}$ precesses and the spin and orbital momentum precesses around $\mathbf{J}$.

As $\mathbf{J}$, and therefore also the magnetization $\mathbf{M}$ precesses, the energies of the states change through variations in the spin-orbit contribution and transitions between states take place. This creates an effective field $\mathbf{H}^{\text{eff, damping}}$ [146]

$$\mathbf{H}^{\text{eff, damping}} = -\frac{1}{\mu_0 |\mathbf{M}|} \sum_{n\mathbf{k}} \left[\rho_{n\mathbf{k}} \frac{\partial \epsilon_{n\mathbf{k}}}{\partial \mathbf{m}} + \frac{\partial \rho_{n\mathbf{k}}}{\partial \mathbf{m}} \epsilon_{n\mathbf{k}} \right], \tag{5.12}$$

where $\epsilon_{n\mathbf{k}}$ is the electron energy with a band index n and spin wavevector $\mathbf{k}$, $\rho_{n\mathbf{k}}$ is the occupation number and $\mathbf{m}$ the unit direction vector of the magnetization $\mathbf{M}$.

The first term between brackets is the variation in the spin-orbit energies as the magnetization changes direction. This effect is normally referred to as the breathing Fermi surface model and gives rise to *intraband* scattering. The second term between brackets accounts for changes in the effective field due to transitions between states and is normally called the bubbling Fermi surface model and gives rise to the *interband* scattering.

5.3.1.1 Intraband scattering

When the magnetization precesses, it generates a time-dependent spin-orbit coupling that can push some occupied states from just below the Fermi energy to above the Fermi energy and vice versa.

In the relaxation time approximation [146] ρ_{nk} can be written as

$$\rho_{n\mathbf{k}} = f_{n\mathbf{k}} - \tau \frac{df_{n\mathbf{k}}}{dt}, \tag{5.13}$$

where $f_{n\mathbf{k}}$ is the equilibrium Fermi-Dirac occupation and τ determines how fast an electron-hole pair relaxes back to an equilibrium state. In the limit $\tau \to 0$, the electrons are scattered so often that the electronic systems is always in the ground state. In Figure 5.5.a, this corresponds to the case where at time t - dt only states in S(t - dt) are occupied and at time t only states in S(t) are occupied.

With a finite relaxation time τ, the scattering processes are not able at each time to create an equilibrium situation for the electronic system and the equilibrium occupation number lags behind the real occupation number. So it could happen that states that should be empty at time t are still occupied and that states that should be occupied are still empty, due to the time lag of the real occupation number. As shown in Figure 5.5.b, this time lag gives rise to the creation of electron-hole pairs.

The intraband damping rate is then equal to [146]

$$\alpha = \tau \frac{\gamma}{\mu_0 M_s} \sum_{n\mathbf{k}} \left(-\frac{df_{n\mathbf{k}}}{d\epsilon_{n\mathbf{k}}} \right) \left(\frac{\partial \epsilon_{n\mathbf{k}}}{\partial \mathbf{m}} \right)^2. \tag{5.14}$$

The damping is proportional to τ, like the electrical Drude conductivity. The intraband scattering is therefore called conductivity-like. In Figure 5.6, the contribution of the intraband scattering for Co along different crystallographic directions is shown with dashed lines.

5.3.1.2 Interband scattering

When the magnetization precesses, it generates a time-dependent spin-orbit coupling. This coupling acts as a time-dependent perturbation that can cause a transition between the states $\psi_{n\mathbf{k}}$ and $\psi_{l\mathbf{k}}$ as shown in Figure 5.5.b. The initial and final state have the same wavevector $\mathbf{k}$, since in FMR experiments the uniform, $\mathbf{k}$ = 0, mode is excited. Using Fermi's golden rule, the transition rate between states $\psi_{n\mathbf{k}}$ and $\psi_{l\mathbf{k}}$ can be calculated.

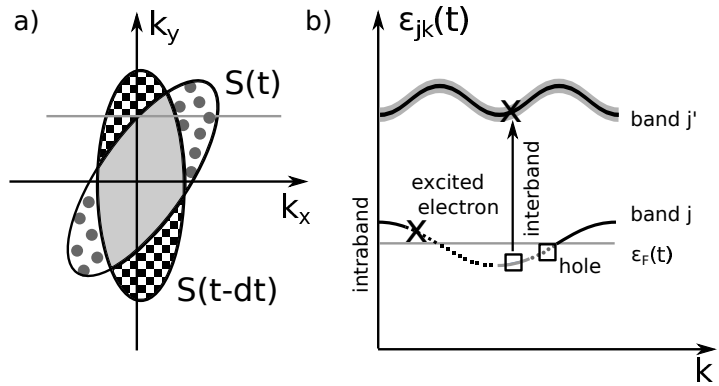

Figure 5.5: a) Sketch of the equilibrium Fermi surface S, taken to be an ellipsoid in this example, at time t (S(t), gray dotted part + light gray center part) and time t - dt (S(t - dt), black squares + light gray middle part). For fast relaxation, the light gray states are occupied the whole time while at time t only the dotted states are occupied and at time t - dt only the squared states are occupied. b) Sketch of the equilibrium band ε_{jk} along the horizontal gray line in a). In a realistic situation, the occupation number lags behind the Fermi-Dirac distribution function and and at time t, some states in the squared Fermi surface are still occupied and some states in the dotted part are still empty. The excited electron-hole pair will relax via an intraband transition. Reprinted with permission from [147]. ©(2010) by the American Physical Society.

The interband damping rate is then equal to [146]

$$\alpha = \frac{\gamma}{2\mu_0 M_s} \sum_{nk} \sum_{l \neq n} W_{ln}(\mathbf{k}) \frac{[\rho_{n\mathbf{k}} - \rho_{l\mathbf{k}}]}{\omega} \frac{[\epsilon_{l\mathbf{k}} - \epsilon_{n\mathbf{k}}]}{\omega} \tag{5.15}$$

where ω is the precession frequency and $W_{ln}(\mathbf{k})$ is the transition rate between states $\psi_{n\mathbf{k}}$ and $\psi_{l\mathbf{k}}$ and equal to

$$W_{ln}(\mathbf{k}) = \frac{2\pi}{\hbar} \left| 2 \left(\frac{\partial \epsilon_{n\mathbf{k}}}{\partial \mathbf{m}} \right)^2 \right|^2 \delta(\epsilon_{l\mathbf{k}} - \epsilon_{n\mathbf{k}} - \hbar\omega). \tag{5.16}$$

There is an energy gap $\Delta\epsilon$ between the states ψ_{nk} and ψ_{lk}. When $\Delta\epsilon > \hbar/\tau$, the Gilbert damping is proportional to $1/\tau$ and scales as the resis-

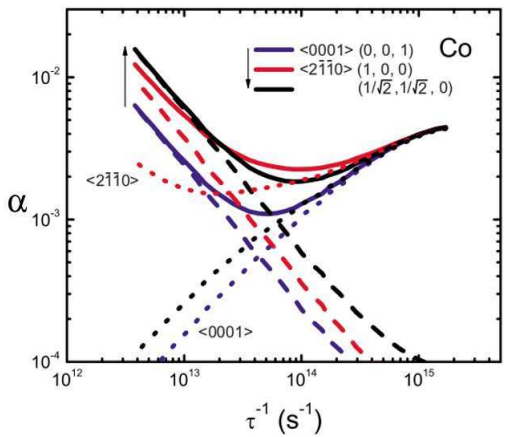

Figure 5.6: Calculated Gilbert damping α for Co. The dotted lines indicate the contribution of the interband scattering to the total scattering, whereas the dashed lines indicate the contribution of the intraband scattering. Figure reprinted with permission from [148]. ©(2007) by the American Physical Society.

tivity. In Figure 5.6, the contribution of the interband scattering for Co along different crystalographic directions is shown with dotted lines.

5.3.2 Other mechanism

The relaxation of a uniform precession mode in a ferromagnet can also happen via indirect damping. The two-magnon process [149] is an example of an indirect damping process, as shown in Figure 5.3. Here, the uniform precession mode ($\mathbf{k} = 0$) scatters into non-uniform modes ($\mathbf{k} \neq 0$).

The damping can also be influenced by eddy currents [138]. Eddy current damping, α_{eddy} is proportional to

$$\alpha_{\text{eddy}} \propto \gamma M_s \sigma d^2, \tag{5.17}$$

where σ is the electrical conductivity, d the film thickness and M_s the saturation magnetization.

5.4 Experimental

The Co(d)/Pt(10) and Co(d)/Cu(10) films, where d is varying and all thicknesses are in nm, were deposited on oxidized Si(100) in a UHV chamber (base pressure 1×10^{-9} mbar) using DC magnetron sputter deposition with argon as plasma at room temperature from 3N5 Co, 3N5 Cu and 3N5 Pt targets. Since the thickness of the Cu- and Pt-layers are not going to be varied and to take into account both interfaces of the Co layer, we call them SiO_x/Co(d)/Cu and SiO_x/Co(d)/Pt. The deposition rate was measured by X-ray reflectivity (XRR) using Cu-Kα radiation and was 0.58 Å/s for Co, 1.90 Å/s for Cu and 1.54 Å/s for Pt respectively. Values of d ranged from 1.5 nm to 50 nm.

Magnetization measurements were performed in a SQUID-based magnetometer (MPMS 5S from Quantum Design). For electrical characterization, the samples were patterned into Hall bar structures, 50 $\times$ 1000 μm^2, using negative resist, electron beam lithography and ion beam etching. Resistivity measurements were performed using the resistivity option with an excitation current of 100 μA in a Physical Properties Measurement System (Quantum Design).

FMR was measured using a Bruker EMXplus X-band spectrometer, see Figure 5.7.a, in a TE_{011} cavity with a maximum DC-field of 0.6 T or with a Bruker E680 ElexSys 9.5 in a TE_{102} cavity with a maximum DC-field of 1.5 T. The 2.4 $\times$ 2.4 mm^2 samples were glued with silverpaint

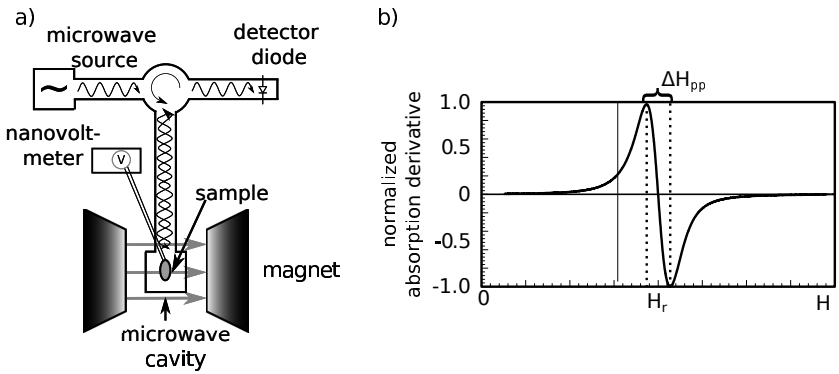

Figure 5.7: a) Schematic of an EPR/FMR measurement set-up. b) FMR spectrum where the normalized derivative absorption is plotted as a function of the applied static magnetic field H, with a resonance field H_r and a peak-to-peak linewidth ΔH_{PP}.

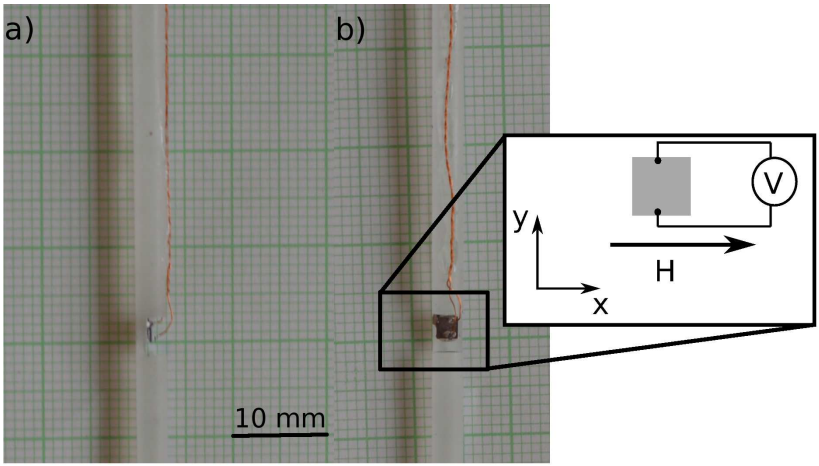

Figure 5.8: Side view (a) and front view (b) of a 2.4 $\times$ 2.4 mm^2 sample mounted on a Rexolite sampleholder with wires glued to the sample for ISHE measurements. The inset shows the orientation of the magnetic field with respect to the sample and the position of the electrical contacts to measure the ISH voltage.

in a notch of a Rexolite 1422 rod as shown in Figure 5.8. The notch was made into the rod, to align the sample on the rotation axis of the rod and in the middle of the cavity. A goniometer was used to rotate the rod in the cavity and to vary the angle θ_H between the applied magnetic field and the film normal. Most measurements were done with 100 kHz modulation frequency and 1 Gauss modulation amplitude. For low temperature measurements, a He flow cryostat was used. The flow cryostat consist of a double walled, vacuum insulated quartz tube that fits in the microwave cavity. The sampleholder is placed into the quartz tube, where just below the sample a thermometer and heater are mounted.

Using cavity based-FMR, the frequency is fixed and the static magnetic field is swept to fulfill the resonance condition. A typical FMR spectrum is shown in Figure 5.7.b. Due to field modulation in combination with lock-in detection, not the microwave absorption is measured, but its first derivative. The peak-to-peak linewidth ΔH_{pp} is the difference between the maximum and minimum intensity of the absorption derivative. ΔH_{pp} is related to the full width half maximum ΔH of the Lorentzian absorption profile as $\sqrt{3}\Delta H_{\mathrm{pp}} = \Delta H$ [150]. The resonance

field H_r is the applied magnetic field H, where the resonance condition is fulfilled. This is visible in the FMR spectrum as the applied field where the absorption derivative is equal to 0.

When also the inverse spin Hall (ISH) voltage was measured, twisted Cu wires were glued with silverpaint, see Figure 5.8.c, to the sample and the ISH voltage was measured using a Keithley 2182a nanovoltmeter.

5.5 FMR measurements

In Figure 5.9, the raw FMR spectra of a SiO_x/Co(2)/Pt bilayer are plotted for different applied field directions θ_H. For an in-plane applied magnetic field ($\theta_H = 90°$), the resonance condition is fulfilled in a small magnetic field and the peak-to-peak linewidth is very narrow. When rotating the sample slowly to the out-of-plane magnetic field configuration ($\theta_H = 0°$), larger magnetic fields are required to fulfill the resonance condition and ΔH_{pp} becomes larger. When the applied field direction is almost in the out-of-plane configuration ($\theta_H = 0°$), the peak-to-peak linewidth becomes again more narrow. As can be seen in Figure 5.9, we are not able to obtain a full FMR spectrum, for θ_H smaller than 2°. The background that appears for the high-field FMR spectra is due to the magnetostriction, which modifies the cavity properties a little bit.

In Figure 5.10.a, the measured and fitted angular dependence of the resonance field of a SiO_x/Co(2)/Pt bilayer is plotted. The angu-

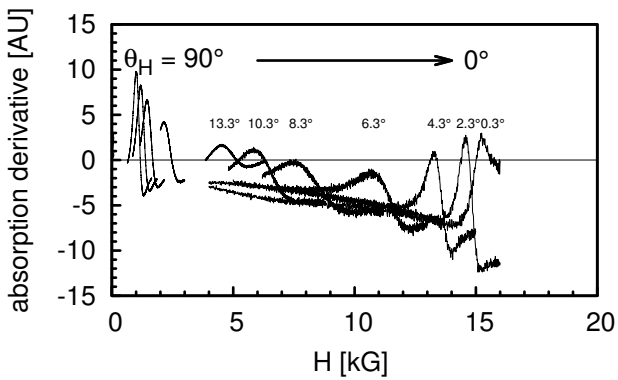

Figure 5.9: Angular dependence of the FMR spectrum of a SiO_x/Co(2)/Pt bilayer for $\theta_H = 90°$ to 0°. For clarity, the angular dependence from $\theta_H = 0°$ to -90° is not plotted.

lar dependence has a peak at $\theta_H = 0°$. The two dotted lines indicate the maximum DC magnetic field the two electromagnets can produce. It should be noted that the actual resonance field at 0° is too large for the 0.6 T and 1.5 T magnet to be measured. Using equations 5.2 and 5.6, the resonance field can be fitted as a function of θ_H. As we are not able to measure the full angular dependence, we fit each curve with a number of g-factors between 1.8 and 2.2. From the fits we extract the average, minimum and maximum value of $4\pi M_{\text{eff}}$ and we obtain for each g-value the angular dependence of the magnetization direction $\theta_M(\theta_H)$. The range for the g-value is chosen between the bulk value for Co, 2.2, and the best fitting g-value for the SiO_x/Co(2)/Pt bilayer, 1.8. A g-value of 1.8 may appear to be low, but both the induced orbital magnetization and the spin pumping effect decrease the g-value. The spin μ_s and orbital μ_l magnetic moments are related to the g-factor via $|\text{g-2}|/2 = \mu_l/\mu_s$ [151]. An induced orbital magnetization will then also change the g-factor. Furthermore, Zhang et al. [152] found using FMR experiments in Si/Ru/20×[Co(25 Å) + Pt(d)]/Pt multilayers, that for a varying Pt thickness d, the g-value varied between 1.83 and 2.30.

In Figure 5.10.b, the fitted angular dependence of θ_M is plotted for the SiO_x/Co(2)/Pt bilayer with a g-value of 1.8. The magnetization direction does not follow directly the direction of the applied magnetic field. From θ_H equal to 90° to almost 10°, the magnetization of the Co film stays in-plane. Around 10°, a sudden change from an in-plane to an out-of-plane magnetization takes place. In Figure 5.10.c, the measured and fitted peak-to-peak linewidth ΔH_{pp} is shown, which exhibits sharp peaks around $\theta_H = \pm 10°$, which corresponds to the change of magnetization direction from in-plane to out-of-plane and a minimum at $\theta_H = 0°$. Furthermore, ΔH_{pp} at θ_H at 0° is larger than ΔH_{pp} at 90°. Using the fitted values for H_r and θ_M, and equations 5.10 and 5.11, also ΔH_{pp} can be fitted. From the fits of ΔH_{pp}, we extract the average, minimum and maximum values of α, $\Delta(\theta_H)$ and $\Delta(4\pi M_{\text{eff}})$.

The angular dependences of the three distinct contributions to the total measured peak-to-peak linewidth are different, as can be seen in Figure 5.10.c. For an in-plane applied magnetic field ($\theta_H = 90°$), the contributions of the Gilbert damping and the spatial variation in the demagnetization field have almost the same size while the contribution from the spatial variation in the crystallographic axis is negligible. Around $\theta_H = 10°$, the contribution in ΔH_{pp} is almost completely determined by the damping due to the spatial variation in the demagnetization field.

In Table 5.1, the average, minimum and maximum fitting parameters are given for a SiO_x/Co(2)/Pt sample when the angular depen-

Table 5.1: Fitting parameters α, $4\pi M_{\text{eff}}$, $\Delta(\theta_H)$ and $\Delta(4\pi M_{\text{eff}})$ of a SiO_x/ Co(2)/Pt bilayer for angular dependent FMR measurements with electromagnets with a maximum field of 0.6 T and 1.5 T magnet. Shown are the average values of 10 fits with different g-factor and the maximum and minimum value from these fits.

	0.6 T magnet			1.5 T magnet			
	average	minimum	maximum	average	minimum	maximum	
α	3.5×10^{-2}	2.0×10^{-2}	6.3×10^{-2}	4.1×10^{-2}	3.3×10^{-2}	4.54×10^{-2}	[-]
$4\pi M_{\text{eff}}$	8.5	6.7	11	10	9.3	11	[kG]
$\Delta(\theta_H)$	0.6	0.0	2	0.03	0.0	1	[°]
$\Delta(4\pi M_{\text{eff}})$	28	14	39	36	34	36	[G]

dence is measured with an electromagnet with a maximum DC field of 0.6 T or 1.5 T. Clearly visible is that the difference between the average and the minimum and maximum values for the 1.5 T magnet is much smaller than for the 0.6 T magnet, but the average values do not deviate too much.

All in all, the damping of these Co films can be described well with the local resonance model, where in addition to the Gilbert damping also the influence of the damping due to the spatial variations in the direction of the crystallographic axis and the demagnetization field should be taken into account. The Gilbert damping value for the 2 nm thick Co layer, 3.5 - 4.1 $\times$ 10^{-2}, has the right order of magnitude (10^{-2}) for a transition-metal ferromagnet [42] and also the variations in the spatial variations in the direction of the easy axis (up to a few degrees) and the demagnetization field (0 - 100 G) show reasonable numbers [153].

In Figure 5.11.a, the normalized room temperature FMR spectra are shown for SiO_x/Co(d)/Pt bilayers with a varying Co thickness d measured with an in-plane field (θ_H = 90°). The FMR spectra are normalized by subtracting the resonance field H_r, which is defined as the magnetic field where the derivative absorption is equal to 0. Also the absorption derivative is normalized by dividing by the maximum measured value of the absorption derivative. In Figure 5.11.b, the resonance fields H_r are plotted for the in-plane (θ_H = 90°) magnetic field as a function of the Co thickness d.

Also in Figure 5.11.b, the peak-to-peak linewidth ΔH_{pp} from the FMR spectra in Figure 5.11.a is plotted as a function of the Co thickness. Clearly visible is that when the Co thickness becomes smaller than 10 nm, the resonance field shifts to a higher value. For films with

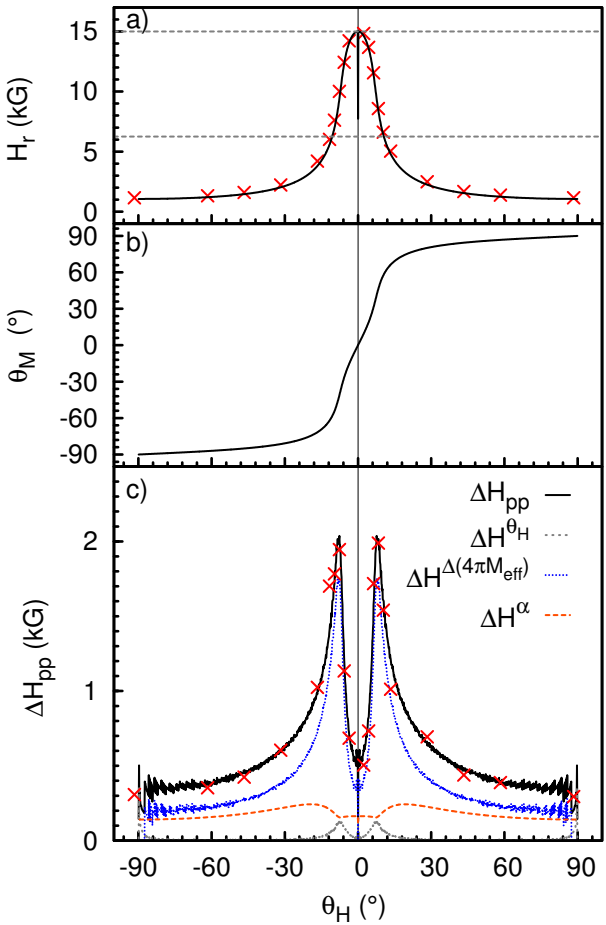

Figure 5.10: a) Angular dependence of the resonance field H_r of a SiO_x/Co(2)/Pt bilayer, where the red crosses (×) represent experimental data and the black line is a fit with a g-factor of 1.80 and M_{eff} of 10.8 kG. The two dotted lines indicate the maximum DC magnetic field the electromagnets can produce. b) The fitted angular dependence of the magnetization direction θ_M as a function of the applied field θ_H. c) Peak-to-peak linewidth of the Co(2)/Pt bilayer. The total peak-to-peak linewidth ΔH_{pp}, black line with the experimental data as red crosses (×), consists of three components: intrinsic damping ΔH^{α} [α = 0.034] and the variation in the direction of the easy axis $\Delta H^{\Delta(\theta_H)}$ [$\Delta(\theta_H)$ = 0.15°] and the demagnetization field $\Delta H^{\Delta(4\pi M_{\text{eff}})}$ [$\Delta(4\pi M_{\text{eff}})$ = 34 G].

a Co layer thicker than 10 nm, the resonance field is nearly constant. Also ΔH_{pp} becomes larger when the Co thickness becomes smaller. For Co thicknesses between 10 and 20 nm, ΔH_{pp} is constant and when the Co thickness is larger than 20 nm, ΔH_{pp} becomes again larger due to eddy current damping. So, for the Co thickness range we measure in this Chapter, we can distinguish three different regimes: for the thin Co films ($d < 10$) we expect that the spin pumping damping mechanism is dominant, for the thick Co films ($d > 20$ nm) we expect that the eddy current damping mechanism is dominant and between these two regimes there is a transition region.

Figure 5.12 shows the effective demagnetization M_{eff} and the saturation magnetization at room temperature for the SiO_x/Co(d)/Pt bilayers. As a reference, the bulk saturation magnetization of Co is indicated. The magnetization of the SiO_x/Co(d)/Pt multilayers was measured by dividing the measured magnetic moment by the measured sample volume (typical 2.4 mm $\times$ 2.4 mm $\times$ d). The error bars of the effective demagnetization field indicate the maximum and minimum values of the parameter in the fit for the range of g-factors. Clearly visible is that the effective demagnetization field becomes smaller, when the Co thickness decreases. Together with the SiO_x/Co(d)/Pt dataset which will be presented in Chapter 6, we see that the saturation magnetization stays nearly constant at a value of approximately 18.8 kG, compared with a value of 17.6 kG for bulk Co.

In Figure 5.13, the average fitting parameters are plotted as a function of the Co layer thickness d. The error bars indicate the maximum and minimum values of the parameter in the fit for the range of g-factors. A clear trend is visible for α. When the Co layer thickness becomes smaller, the Gilbert damping α increases. Furthermore, $\Delta(\theta_H)$ and $\Delta(4\pi M_{\mathrm{eff}})$ are almost constant for Co thicknesses larger than 7.5 nm, but become somewhat larger for Co thicknesses smaller than 7.5 nm.

5.6 Spin pumping detected by the inverse spin Hall effect

Using the inverse spin Hall (ISH) effect, the spin current generated by the spin pumping can be electrically detected. Figure 5.8.b shows how the electrical contacts are made to the sample and the orientation of the contacts with respect to the sample and the applied magnetic field.

In Figure 5.14, the FMR spectrum and the electrically measured voltage V_m of a SiO_x/Co(25)/Pt bilayer are plotted. It is known [154] that

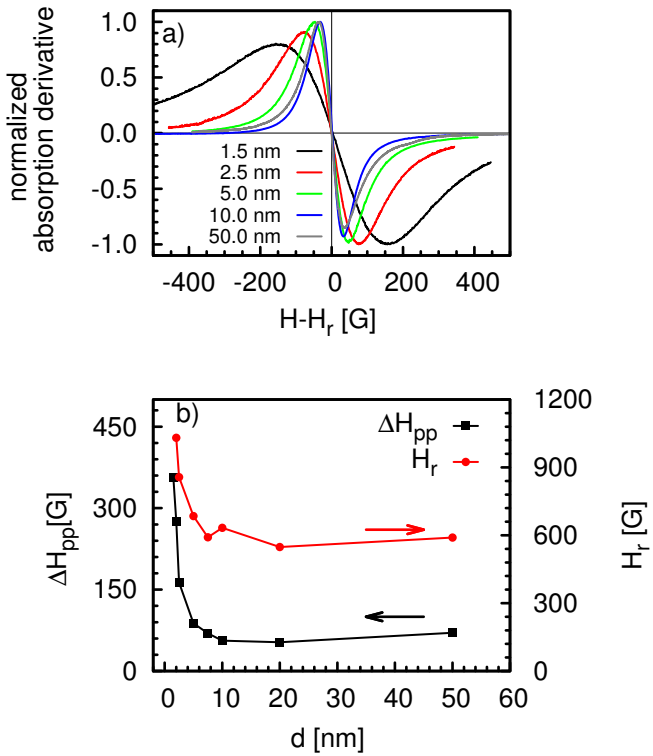

Figure 5.11: a) Normalized in-plane FMR spectra, measured at $\theta_H = 90°$, for a SiO_x/Co(d)/Pt films, where the thickness d of the Co films was varied. The horizontal axis is the normalized dc magnetic field, where the H_r, red ●, for each film is shown in b). In b), also the linewidth of the FMR spectra, black ■, as a function of the Co thickness d is shown.

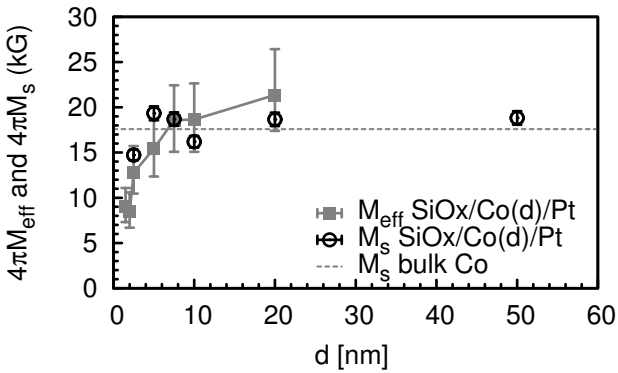

Figure 5.12: The effective demagnetization $4\pi M_{\text{eff}}$ (gray ■)and the saturation magnetization $4\pi M_s$ (black ○), as a function of the thickness d of the Co layer in the SiO_x/Co(d)/Pt multilayer. The dotted line shows the saturation magnetization of bulk Co.

the lineshape of V_m consists of two parts. One is symmetric and a combination of the ISH voltage and the anomalous magnetoresistance effect (AMR). The other is antisymmetric and originates from the anomalous Hall effect (AHE), generated by the electric field component of the applied microwave field. By fitting a Lorentian lineshape V_s and the derivative of a Lorentian lineshape V_a, the symmetric and antisymmetric contributions can be separated. The ISH and the AMR effects in the symmetric lineshape can be distinguished by an inversion of the applied magnetic field. The ISH effect changes sign when the direction of the applied magnetic field is inverted, but the contribution due to the AMR does not change sign [70]. For the rest of the measurements, the symmetric part of the measured voltage is shown and called the ISH voltage V_{ISH}.

In Figure 5.15.a, the ISH voltage is plotted as a function of the applied magnetic field for different field angles θ_H. Clearly visible is that for an in-plane applied field (θ_H = 90° and 270°), the resonance condition is fulfilled with a small magnetic field. When rotating the sample slowly to an out-of-plane orientation (θ_H = 0° and 180°), the V_{ISH} curve moves to a higher magnetic field. The value of the measured maximum ISH voltage of each curve does not change when the field angle is varied as shown in Figure 5.15.b. We cannot measure V_{ISH} close to the out-of-plane orientation, because our magnet cannot produce a large enough magnetic field to fulfill the resonance condition. This results in

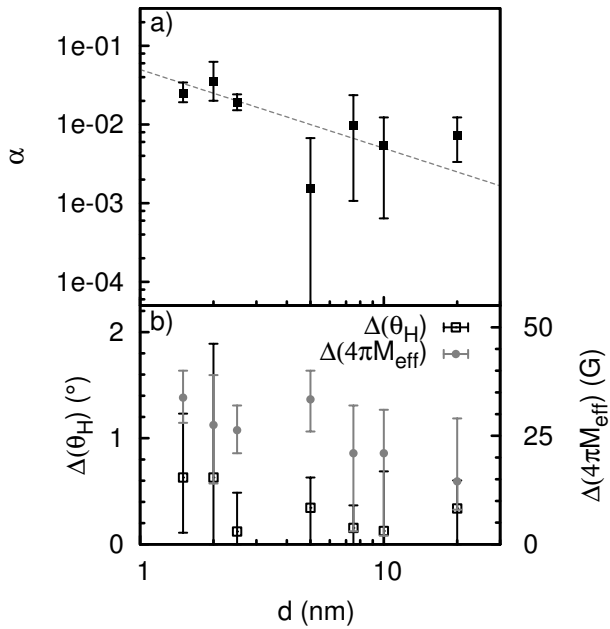

Figure 5.13: a) The damping α, black ■ and in b) $\Delta(\theta_H)$, black □, and $\Delta(4\pi M_{\text{eff}})$, gray •, as a function of the thickness d of the Co layer in the SiO_x/Co(d)/Pt bilayers. Shown are the average values of 10 simulations with different g-factor and the maximum and minimum value from these simulations. The dashed line shows a $1/d$-dependence as a guide to the eye.

an abrupt jump of V_{ISH} at angles close to the out-of-plane orientations (θ_H = 0° and 180°). Furthermore, it is visible that V_{ISH} changes sign when the direction of the applied field is changed. This indicates that the measured symmetric component is only due to the ISH voltage.

The angular dependence of V_{ISH} is given by [155]

$$V_{\text{ISH}} \propto \frac{\sin\theta_M \left[\frac{H_r}{4\pi M_s}\cos(\theta_M-\theta_H)-\cos 2\theta_M\right]}{\left[2\frac{H_r}{4\pi M_s}\cos(\theta_M-\theta_H)-\cos\theta_M-\cos^2\theta_M\right]^2}. \tag{5.18}$$

Using the fitted values of θ_M and H_r from the angular dependent FMR fit, we plot equation 5.18 in Figure 5.15.

In Figure 5.16.a, V_{ISH} of a SiO_x/Co(25)/Pt bilayer is plotted as a function of the applied microwave power P_{RF} for θ_H = 90°. With in-

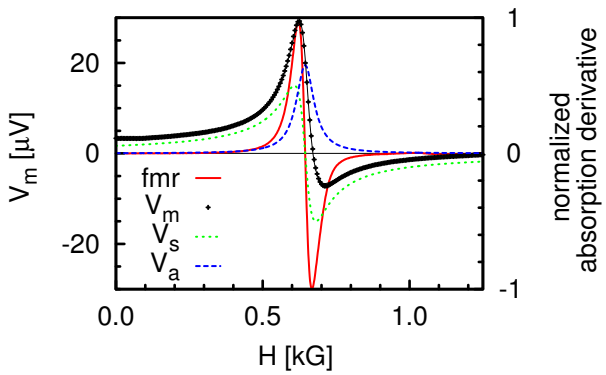

Figure 5.14: The electrically detected voltage V_m of a SiO_x/Co(25)/Pt bilayer is shown as a function of the applied magnetic field H. As a reference, also the FMR spectrum is shown. The measured voltage V_m consist of a symmetric V_c and antisymmetric V_a part, which can be obtained by fitting a Lorentzian and a derivative of a Lorentzian to the measured voltage V_m.

creasing P_{RF}, V_{ISH} increases. V_{ISH} scales linearly with the applied microwave power, as is shown in Figure 5.16.b.

In Figure 5.16.c, V_{ISH} at 158.9 mW is plotted as a function of the thickness of the Co layer. For thin Co films, V_{ISH} increases linearly with the thickness of the Co layer. We measured a maximum voltage for the Co layer with a thickness of 25 nm and for the next measured Co thickness (50 nm), we observe a decrease. The measured V_{ISH} as a function of the thickness of the normal metal d_N and ferromagnet d_F layer is described by [156]

$$V_{\mathrm{ISH}} = L\frac{2e/\hbar}{\sigma_N(d_N)d_N + \sigma_F(d_F)d_F}\left[j^z_{1s}(0)\alpha_{\mathrm{SHE,N}}l_{\mathrm{SD,N}}\tanh\frac{d_N}{2l_{\mathrm{SD,N}}} + j^z_{2s}(0)\alpha_{\mathrm{SHE,F}}l_{\mathrm{SD,F}}\tanh\frac{d_F}{2l_{\mathrm{SD,F}}}\right], \tag{5.19}$$

where L is the distance between the two voltage contacts, $\sigma_i(d_i)$ an $\alpha_{SHE,i}$ are the thickness dependent conductivity and the spin Hall angle of the normal metal or ferromagnet respectively and $j^z_{1s}(0)$ and $j^z_{2s}(0)$ are the spin currents at the normal and ferromagnetic side of the interface respectively. The first term in the brackets represents the backflow from the spin current from the spin sink. If the thickness of

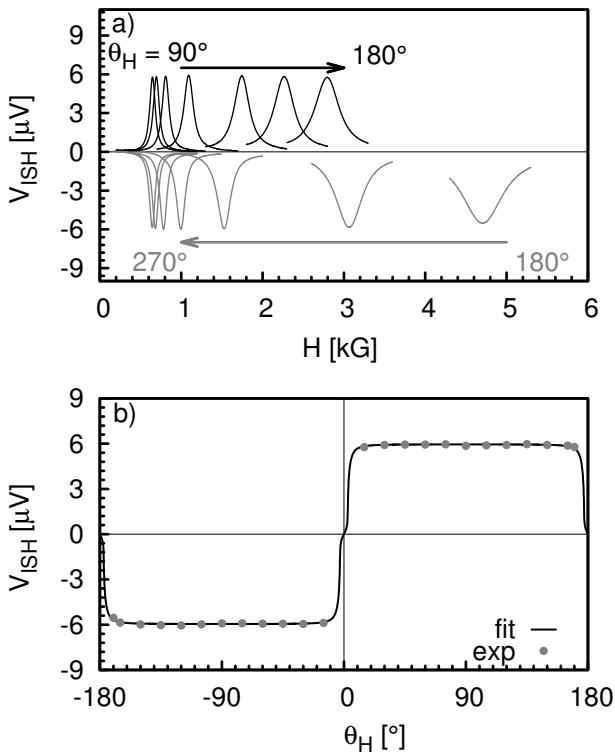

Figure 5.15: a) Field dependence of the inverse spin Hall voltage V_{ISH} of a SiO_x/Co(10)/Pt bilayer for different field angles θ_H, where at 90° and 270° the applied magnetic field is in-plane and at 0° and 180° the applied magnetic field is out-of-plane. b) Inverse spin Hall voltage as a function of the field angle θ_H plotted together with equation 5.18.

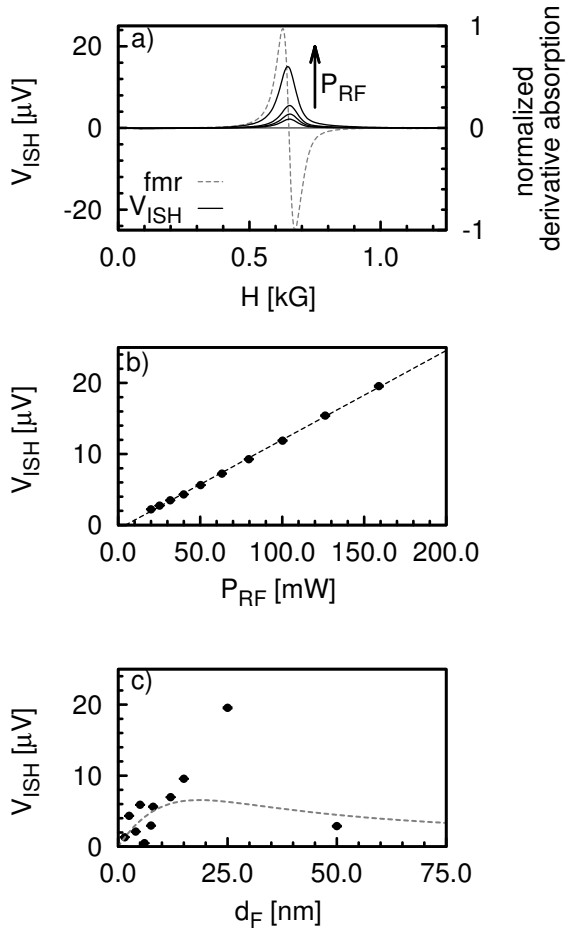

Figure 5.16: a) The inverse spin Hall voltage V_{ISH} of a SiO_x/Co(25)/Pt bilayer as a function of the applied microwave power P_{RF} for θ_H = 90°. Also the measured FMR spectrum of the SiO_x/Co(25)/Pt bilayer is shown. b) The measured V_{ISH} of the SiO_x/Co(25)/Pt bilayer as a function of the applied microwave power. c) The maximum measured V_{ISH} (P_{RF} = 158.9 mW and θ_H = 90°) as a function of the thickness of the ferromagnet d_F plotted together with equation 5.19.

the spin sink is not larger than twice the spin diffusion length, the spin sink cannot be described as ideal, since not all the spin current is absorbed. The second term in the brackets describes the spin current in the ferromagnet. When the thickness of the ferromagnet is smaller than the spin diffusion length in the ferromagnet, the spin current in the ferromagnet will vanish. In Figure 5.16.c, equation 5.19 is plotted for a set of parameters which mimics the measured behaviour of V_{ISH} as a function of the Co thickness. Clearly visible is that for small Co thicknesses, V_{ISH} increases since $d_F < l_{\mathrm{SD,F}}$. When the thickness of the Co increases, the $1/d_F$ contribution becomes larger and V_{ISH} decreases again.

The measurements shown in this section demonstrate that spin pumping is present in the SiO_x/Co/Pt multilayers. However, an accurate description of the size of the measured ISH voltages is not straightforward, as many material dependent fitting parameters are not (well) known in the literature for ultrathin films and the parameters known depend strongly on how the films are grown [157, 158].

5.7 Low temperature electrical characterisation

Before measuring low temperature FMR spectra on the SiO_x/Co/Pt and SiO_x/Co/Cu bilayers, the electrical properties of the used metals were measured. In Figure 5.17, the normalized resistance of a 50 nm thick Co, Pt and Cu and a SiO_x/Co(10)/Pt Hall bar are plotted. No anomalies are visible and the residual resistance ratios (RRR) are 2.76, 1.96 and 1.26 for the 50 nm thick Cu, Co, Pt film and 1.50 for the SiO_x/Co(10)/Pt bilayer.

5.8 Low temperature spin pumping

Figure 5.18 shows the temperature dependence of the normalized peak-to-peak linewidth ΔH_{pp} (a) and resonance field H_r (b) of a SiO_x/Co(10)/Cu and a SiO_x/Co(10)/Pt thin films that were measured with an in-plane (θ_H = 90°) applied magnetic field. Both ΔH_{pp} and H_r are normalized by dividing the measured values by the measured values at 290 K. The peak-to-peak linewidths of both the SiO_x/Co(10)/Cu and the SiO_x/Co(10)/Pt films increase when decreasing the temperature until the maximum is reached. For the SiO_x/Co(10)/Cu samples the maximum was measured at 40 K and ΔH_{pp} was 1.5 times as large the one measured at 290 K. For the SiO_x/Co(10)/Pt sample the maximum was measured at 30 K and ΔH_{pp} was 1.7 times as large as the one measured at 290 K. When decreasing the temperature even further,

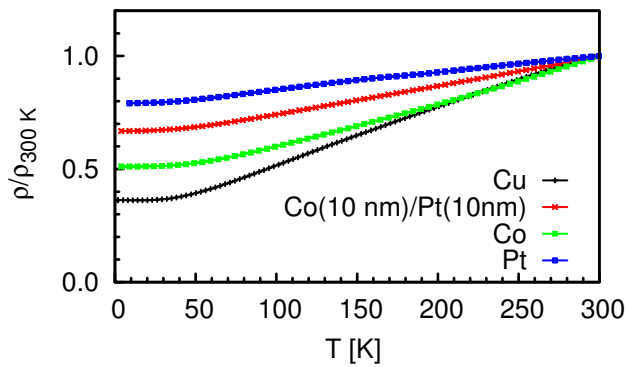

Figure 5.17: a) Normalized resistivity of Co(50), Cu(50), Pt(50) and SiO_x/Co(10)/Pt Hallbar as a function of temperature. The resistivity at 300 K is 175, 30, 2315 and 927 nΩm for Cu, Co, Pt and SiO_x/Co(10)/Pt respectively.

the linewidth becomes narrower again. The measured resonance field in Figure 5.18.b shows a different behaviour. For the SiO_x/Co(10)/Cu samples H_r remains constant over the whole measured temperature range, whereas H_r of the SiO_x/Co(10)/Pt sample increases when decreasing the temperature and becomes almost constant below 100 K.

To gauge whether the contributions of the sample inhomogeneities and the intrinsic relaxation to the total damping change, the angular dependence of a SiO_x/Co(10)/Pt bilayer was measured at 30 K and 300 K. In Table 5.2, the average, minimum and maximum fitting parameters are shown. When decreasing the temperature, all four fitting parameters become larger. The three parameters involving the damping, α, $\Delta(\theta_H)$ and $\Delta(4\pi M_{\text{eff}})$, all becomes approximately 1.8 times as large.

As discussed in Section 5.3.1, theoretical models calculate the damping as a function of scattering time τ and distinguish two cases; intraband scattering which is proportional to τ and interband scattering which is proportional to $1/\tau$. The temperature dependence of the scattering rate is not well known, but from the scattering rate the resistivity can be calculated straightforwardly. Gilmore [146] calculated the damping as a function of the resistivity, where he assumed that the resistivity is dominated by electron-lattice interactions and that electron-electron interactions play a minimal role. He predicts then that the

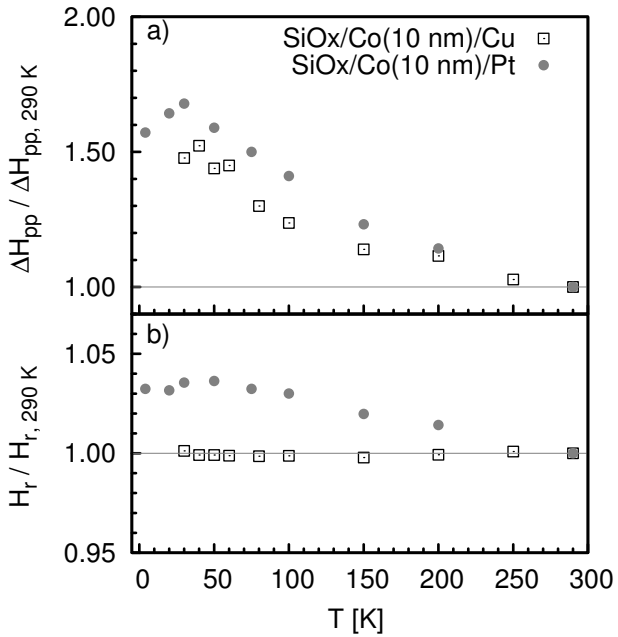

Figure 5.18: a) Normalized in-plane (θ_H = 90°) peak-to-peak linewidth ΔH_{pp}, for a SiO_x/Co(10)/Pt (gray •) and SiO_x/Co(10)/Cu (black ⊡) bilayer as a function of temperature. ΔH_{pp} is normalized by dividing the measured values by the measured ΔH_{pp} at 290 K. ΔH_{pp} at 290 K was 35 G for the SiO_x/Co(10)/Cu bilayer and 56 G for the SiO_x/Co(10)/Pt bilayer respectively. b) Normalized resonance field H_r for a SiO_x/Co(10)/Pt and a SiO_x/Co(10)/Cu bilayer as a function of temperature. H_r is normalized by dividing the measured values by H_r at 290 K. H_r at 290 K was 572 G for the SiO_x/Co(10)/Cu bilayer and 633 G for the SiO_x/Co(10)/Pt bilayer respectively.

Table 5.2: Fitting values for the damping α, $4\pi M_{\text{eff}}$, $\Delta(\theta_H)$ and $\Delta(4\pi M_{\text{eff}})$ for fitting of the measured values of a SiO_x/Co(10)/Pt bilayer at 300 K and 30 K. Shown are the average values of 10 simulations with different g-factor and the maximum and minimum value from this simulations.

	300 K			30 K			
	average	minimum	maximum	average	minimum	maximum	
α	6.62×10^{-3}	3.94×10^{-3}	1.23×10^{-2}	1.23×10^{-2}	8.90×10^{-3}	1.71×10^{-2}	[-]
$4\pi M_{\text{eff}}$	18.7	15.1	22.7	19.9	16.3	24.3	[kG]
$\Delta(\theta_H)$	0.13	0	0.71	0.23	0	0.43	[°]
$\Delta(4\pi M_{\text{eff}})$	21	20	31	38	30	53	[G]

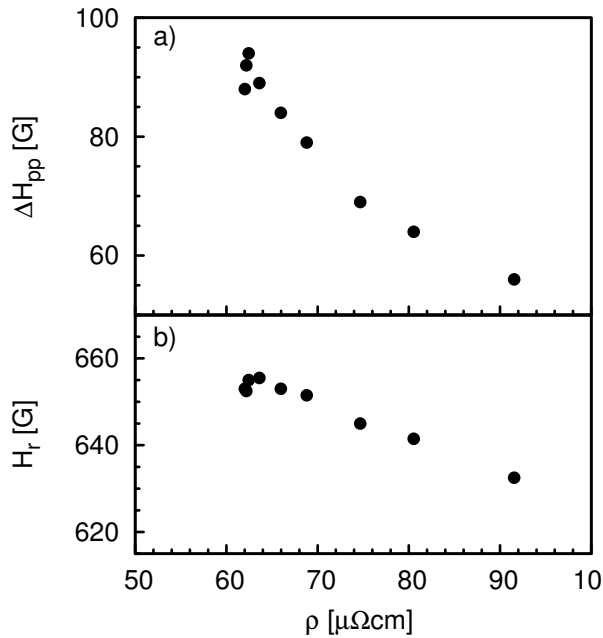

Figure 5.19: In-plane (θ_H = 90°) peak-to-peak linewidth ΔH_{pp} (a) and resonance field H_r (b), for a SiO_x/Co(10)/Pt bilayer as a function of the resistivity.

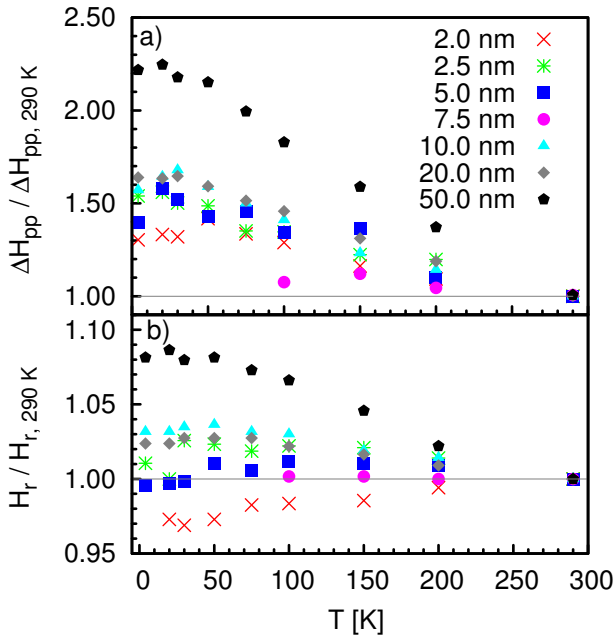

Figure 5.20: a) Normalized in-plane (θ_H = 90°) peak-to-peak linewidth ΔH_{pp} for SiO_x/Co(d)/Pt bilayer as a function of temperature. ΔH_{pp} is normalized by dividing the measured values by the measured values at 290 K. b) Normalized resonance field H_r for SiO_x/Co(d)/Pt films as a function of temperature. H_r is normalized, by dividing the measured values by the measured values at 290 K. ΔH_{pp} and H_r at 290 K can be found in Figure 5.11.b.

damping changes from the intraband to the interband scattering mechanism around a resistivity of approximately 1–100 $\mu\Omega$cm, dependent on the lifetimes of the spin-up versus spin-down states.

By plotting ΔH_{pp} as a function of the resistivity, experimental data can be compared with these theoretical predictions. Figure 5.19 shows how ΔH_{pp} and H_r of the SiO_x/Co(10)/Pt bilayer vary as a function of the resistivity. The resistivity of the bilayer is measured with a different SiO_x/Co(10)/Pt bilayer, that was patterned into a Hall bar. Both show a monotonic increase with a maximum at a resistivity of 63 $\mu\Omega$cm. Below this value, both ΔH_{pp} and H_r decrease.

Figure 5.20.a shows how the measured and normalized ΔH_{pp} of all

SiO_x/Co(d)/Pt bilayers (shown in Figure 5.18 for d = 10 nm) changes as function of the Co layer thickness. The normalization values can be found in Figure 5.11.b. Most bilayers show similar behaviour to what was seen for the SiO_x/Co(10)/Pt bilayer in Figure 5.18.a. When decreasing the temperature, the linewidth becomes broader up to a certain temperature. For the films with a Co-layer thinner than 20 nm, the maximum linewidth is approximately 1.3 to 1.7 times as large as the linewidth at 290 K and the linewidth of the sample with the 50 nm thick Co layer becomes even 2.2 times as large. For all samples that were measured in the full temperature range, the maximum ΔH_{pp} was found around 20 to 30 K.

In Figure 5.20.b, the normalized resonance fields of the SiO_x/Co(d)/Pt bilayers are plotted as a function of temperature. The normalization values can be found in Figure 5.11.b. Three things can be observed. First, H_r of the SiO_x/Co(50)/Pt bilayer increases when the temperature is decreased and the maximum measured increase is almost 1.1 times. The maximum H_r of all the other measured samples does not become larger than 1.05 times the resonance field at 290 K. Secondly, H_r of the SiO_x/Co(2.5)/Pt bilayer becomes smaller than the H_r at 290 K. This happens also for the SiO_x/Co(5)/Pt bilayer, but only at low temperatures. H_r of the other bilayers show similar behaviour as the SiO_x/Co(d)/Pt bilayer in Figure 5.18.b. When decreasing the temperature, H_r becomes larger and after a certain temperature H_r stays almost constant.

In Figure 5.21, ΔH_{pp} is plotted for different temperatures as a function of the thickness d of the Co-layer in the SiO_x/Co(d)/Pt bilayers. The thick Co film (d = 50 nm) shows a large increase in the damping. When decreasing the Co thickness, an increase in the peak-to-peak linewidth can be observed, as is predicted by equation 2.19. This increase in linewidth behaves the same at all the measured temperatures.

5.9 Discussion

The question raised in the beginning of this Chapter was whether we can show the presence of a spin pumping effect in SiO_x/Co/Pt bilayers and find its temperature dependence. For this, the peak-to-peak linewidths ΔH_{pp} in FMR experiments were measured and analyzed in order to separate intrinsic and extrinsic effects. From these data a number of conclusions can be drawn, which will be done below. We separate this in different parts. In the first part, we discuss the dependence of ΔH_{pp} on the Co-thickness, which is a signature of spin pumping.

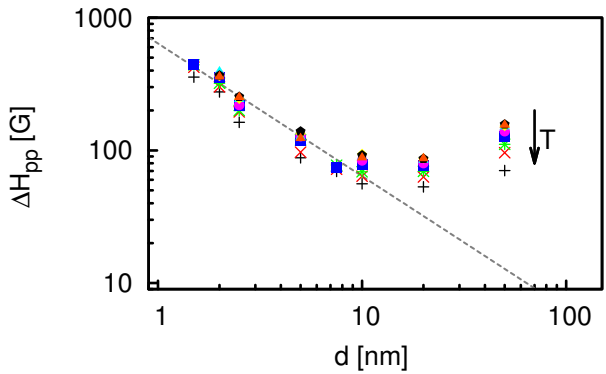

Figure 5.21: Peak-to-peak linewidth ΔH_{pp} as a function of the thickness d of the SiO_x/Co(d)/Pt bilayers for different temperatures. The direction of the arrow indicates an increase in temperature. The dashed line shows a $1/d$-dependence as a guide to the eye.

Next we discuss reasons for the peculiar temperature dependence of ΔH_{pp}. Then, in the course of the analysis, values for the saturation magnetization $4\pi M_s$ and the effective demagnetization fields $4\pi M_{\text{eff}}$ were extracted, which will be discussed as well.

5.9.1 Dependence of ΔH_{pp} on Co-thickness

The main experimental findings here are that ΔH_{pp} at room temperature shows for thin Co thicknesses, $d < 10$ nm, a $1/d$ dependence (see Figure 5.11.b). Furthermore, after separating the various contributions to ΔH_{pp}, the Gilbert damping α is also found to show a 1/d dependence for small Co thicknesses, $d < 10$ nm (see Figure 5.13.a). The larger uncertainty in the latter statement is caused by uncertainty introduced in the separation procedure. The $1/d$-dependence is a characteristic of spin-pumping [67].

The observed angular dependence of the inverse spin Hall voltage V_{ISH} of the SiO_x/Co/Pt bilayers, as shown in Figure 5.15, gives further confirmation that the spin pumping is present. Also the observed thickness dependence of V_{ISH}, as shown in Figure 5.16.c, satisfies the expected behaviour that the measured V_{ISH} increases with a increasing thickness of the ferromagnet until a certain thickness, whereafter V_{ISH} decreases rapidly. We choose however not to use the measured V_{ISH} as a probe to study the temperature dependence of the spin pumping ef-

fect, since it depends on many temperature dependent parameters such as the conductivity, the spin diffusion length and the Gilbert damping, where the latter two have not been systematically measured as a function of temperature.

In order to characterize the low temperature behaviour, we chose to measure the in-plane (θ_H = 90°) ΔH_{pp}. To gauge whether the ratio of intrinsic and extrinsic contributions changed at low temperatures, the angular dependence of the FMR spectra was measured for one SiO_x/Co(10)/Pt bilayer at 300 K and 30 K. In Table 5.2 it is shown that the ratio of the contribution of the intrinsic relaxation and the relaxation due to sample inhomogeneities stays the same. Figure 5.21 shows that the dependence of ΔH_{pp} on d is the same for all temperatures. Together, it feels safe to conclude that also for α there is no change in the room temperature and low temperature thickness dependence, while the value of α has increased by about a factor of 1.8.

The spin pumping theory says that the change in the Gilbert damping is caused by the effective spin mixing conductance $A_{\mathrm{eff}}^{\uparrow\downarrow}$, where in diffusive bilayers $A_{\mathrm{eff}}^{\uparrow\downarrow}$ is governed by the conductivity $\sigma(T)$ of the normal metal layer. The data presented here confirms this picture. However, the temperature dependence of ΔH_{pp} of the SiO_x/Co(d)/Pt bilayers as shown in Figure 5.20.a, behaves as a non-monotonously increasing function, and this cannot be explained using the spin pumping theory.

5.9.2 Dependence of ΔH_{pp} on temperature

The temperature dependence of ΔH_{pp} of both the SiO_x/Co(10)/Pt and SiO_x/Co(10)/Cu, given in Figure 5.18, shows that the ΔH_{pp} is not a monotonously increasing or decreasing function. ΔH_{pp} increases by about a factor of 1.6 when decreasing the temperature until the maximum is reached, around 30 - 40 K.

Experiments on single crystal Co whiskers [42, 142] with a residual resistance ratio (RRR) value between 80-150 showed that ΔH_{pp} increased when the temperature is decreased and saturates at approximately 30 K, where ΔH_{pp} is approximately 3.5 times larger than the linewidth at 300 K. Lloyd and Bhagat [141] showed furthermore, that when alloying Ni with 5 % Cu and thereby reducing the RRR from 30 to 3, no temperature dependence was observed for the linewidth. They attribute the increase in linewidth to a possible increase of the mean free path of the conduction electrons. Also Bastian and Biller [159] measured the temperature dependence of the damping in a Ni-Fe al-

loy. Already with a Fe concentration of 6 %, the increase in linewidth at low temperatures disappeared. They attribute this disappearing of the peak at low temperatures to a decrease of τ by approximately 1 order of magnitude, when alloying the Ni with 6 % Fe.

It is rather surprising that we observe the same behaviour in very thin polycrystalline films with a RRR of just 2 as in single crystal whiskers, since the amount of disorder (where the RRR indicates the amount of disorder) determines both the resistivity and the Gilbert damping.

Czeschka et al. [70] observed the same behaviour for ΔH_{pp} of a SiO_x/Co(10)/Pt(7) bilayer. However, in their measurement H_r becomes smaller for temperatures below 100 K. They attribute both effects to a change in the magnetic anisotropy due to a temperature dependent strain.

In the literature, there are several theories that describe the low temperature behaviour on a phenomenological level via the magnetoelastic coupling between the magnetization and the lattice strain [160]. We choose a different explanation however, observing that the damping is closely linked to the conductivity. As explained in Section 5.3.1, in particular intraband and interband scattering have a different dependence on the conductivity. In Figure 5.19, ΔH_{pp} is plotted as a function of the resistivity. We propose that the maximum in this plot is due to the crossover from intraband scattering at high resistivity (high temperature) to interband scattering at low resistivity (low temperature). Note that a connection to phonons is less likely, since Bastian and Biller [159] found the maximum of their Ni whisker around room temperature. Also the lack of thickness dependence of the ΔH_{pp} as shown in Figure 5.20, makes clear that surface scattering of the Fuchs-Sondheimer type [161, 162] does not play an important role.

ΔH_{pp} in Figure 5.20.a shows for Co thicknesses thinner than 20 nm the same behaviour as the SiO_x/Co(10)/Pt bilayer. ΔH_{pp} of the SiO_x/Co(50)/Pt sample becomes much larger when decreasing the temperature. For Co layers of this thickness, the main damping mechanism is not spin pumping anymore, but eddy current damping. Eddy current damping scales with the conductivity and the conductivity increases with a factor of 1.6 as can be seen in Figure 5.17. The total damping of the 50 nm thick film consists then of intrinsic damping, which increases approximately a factor 1.6 when going to low temperatures and the eddy current damping, that also increases a factor 1.6 when decreasing the temperature. The total damping increases then approximately a factor 2.2 when decreasing the temperature, which agrees very well with the observed broadening in Figure 5.20.a.

5.9.3 Comparison between Co/Pt and Co/Cu

This Chapter was mainly concerned with SiO_x/Co/Pt bilayers, and it was explained that the line broadening with decreasing Co thickness is due to the spin pumping effect, caused by the spin-flip scattering (spin-sinking) of the Pt layer. A less strong scattering material such as Cu could be expected to yield less, or no, broadening effects with decreasing Co thickness. Such a comparison was made with samples of SiO_x/Co(10)/Pt and SiO_x/Co(10)/Cu. We chose bilayers with a 10 nm thick Co layer, because the Co thickness should be far enough away from the region were we expect that the different spin-orbit torques plays an important role in the magnetization dynamics [14, 54–57]. Furthermore, the Co thickness should not be too thick, otherwise the contribution of the spin pumping effect becomes too small.

For the SiO_x/Co(10)/Cu and SiO_x/Co(10)/Pt multilayers, ΔH_{pp} at room temperature is 35 and 56 G respectively, where we contribute the difference in linewidth due to spin pumping in a good and bad spin sink. In Figure 5.18.a, the temperature dependence of the normalized ΔH_{pp} is plotted for both bilayers. The temperature dependence shows that ΔH_{pp} behaves the same for the SiO_x/Co/Pt and SiO_x/Co/Cu bilayers. This is in agreement with the observation in the previous section, where we contribute the low temperature ΔH_{pp} behaviour to a crossover from interband scattering to intraband scattering.

5.9.4 Saturation magnetization, effective demagnetization field and resonance field

The room-temperature saturation magnetization, as shown in Figure 5.12, shows an average saturation magnetization of 18.8 kG. This is larger than the saturation magnetization of bulk Co, 17.6 kG. On top of the Co thin film is a Pt layer. Pt is non-magnetic, but it almost satisfies the Stoner criterion for the onset of ferromagnetism. From literature, it is known that at the Co/Pt interface Co can induce a magnetic moment into Pt [163].

In particular, X-ray resonant magnetic scattering (XRMS) [163] and magnetic circulair X-ray dichroism (XMCD) [164] has been used to show that magnetic moments are induced on the Pt atoms and that the orbital magnetic moment of the Co atoms at the interface increases due to the Co 3d-Pt 5d interfacial hybridization.

The data indicate that up to 0.3 nm, the induced Pt 5d magnetization is 0.2 μ_B per Pt atom, which introduces an extra magnetization of 1.2 kG. The room-temperature saturation magnetization of the Co that

we measured for the Co/Pt bilayers when corrected for the induced magnetization in the Pt layer, is then 17.6 kG, which compares well with the bulk saturation magnetization value for Co.

The saturation magnetization for the Co/Pt bilayer with a 2.5 and 10 nm thick Co layer shows a slightly lower value, which is probably due to the uncertainty in the thickness of the Co film. Another indication for uncertainty in the thickness is seen in Figure 5.11.b, where H_r of the SiO_x/Co(10)/Pt bilayer is larger than H_r of the SiO_x/Co(7.5)/Pt bilayer, which suggest that the 10 nm thick Co layer is thinner than the 7.5 nm thick Co layer. However, ΔH_{pp} of the SiO_x/Co(10)/Pt is not larger than ΔH_{pp} of the SiO_x/Co(7.5)/Pt, which suggest that the 10 nm Co layer is thicker than the 7.5 nm Co layer. It is not clear what causes this anomaly.

The temperature dependence of H_r (see Figure 5.18.b) of the bilayers with a Co thickness between 5 and 20 nm can be explained by a lower Curie temperature of the CoPt alloy at the interface of the Co/Pt bilayer. The behaviour of the resonance field for the SiO_x/Co/Pt with a thickness of the Co layer less than 5 nm is unexpected and we tentatively attribute this decrease of the resonance field to the temperature dependence of the Rashba spin-orbit torque (see Chapter 6).

The temperature dependence of H_r of the SiO_x/Co(10)/Pt(7) bilayer of Czescka et al. [70] shows a different trend, as H_r becomes smaller with decreasing temperatures. The big difference between their samples and our samples is the growth method. Their samples were grown using the evaporating technique, that should result in more sharp interfaces and a different grain size than our samples that were grown using the sputtering technique [158].

In Figure 5.12, $4\pi M_{\text{eff}}$ becomes smaller as the Co thickness decreases. From the magnetization measurements, the saturation magnetization for the SiO_x/Co(d)/Pt is almost constant for decreasing thickness d of the Co layer. As $4\pi M_{\text{eff}}$ is equal to $4\pi M_s$ - $H_\perp$, the perpendicular anisotropy $H_\perp$ increases for the thinner Co thicknesses as has been shown with magnetization [165], MCXD [164] and XRMS [163] measurements. This decrease of $4\pi M_{\text{eff}}$ can also be observed as an increase of the resonance fields as function of the thickness of the Co layers. For very thin Co layers, also other physical mechanisms, that are discussed in Chapter 6, contribute to the increase of the resonance field.

5.10 Summary

We conclude this Chapter by summarizing the main results as they emerge from the discussion. We measured the temperature dependence of the FMR spectra from SiO_x/Co(d)/Pt bilayers for varying thicknesses d of the Co film. When decreasing the temperature, the saturation magnetization of the SiO_x/Co/Pt bilayer increases due to an induced magnetic moment in the Pt and we observe that the intrinsic scattering mechanism changes from the intraband to the interband transition. Our main result is that the spin pumping mechanism is a temperature independent phenomenon.